

Crack initiation in clay observed in beam bending

N. I. THUSYANTHAN*, W. A. TAKE†, S. P. G. MADABHUSHI and M. D. BOLTON

Tensile cracking in clay is an important phenomenon that affects the strength and permeability of clays in many facilities, such as dams, embankments and landfill liners, as well as being a precursor to slope failures in the natural terrain. This study investigates the stress–strain criteria for cracking in clays by performing four-point bending tests on consolidated kaolin clay beams. Load-controlled and strain-controlled tests were performed on clay beams with varying initial suction to understand the stress–strain criteria for crack initiation in clay. At no stage was the negative pore pressure permitted to exceed the air entry value of the clay, so the clay remained saturated throughout. Strains in the clay were obtained by particle image velocimetry analysis of digital images of the clay beam, and suction measurements were obtained from pore pressure and tension transducers installed within the clay beams. Results from this investigation showed that the threshold tensile strain to cracking in kaolin clay decreased from about 4% at an initial mean effective stress of 15 kPa to about 1.5% at an initial mean effective stress of 100 kPa. The extreme fibre stress at failure of the clay beams indicated an effective tensile strength that was a fraction, dropping from 0.27 to 0.11 of the preconsolidation pressure as the overconsolidation ratio increased from about 2 to about 20. Alternatively, the tensile strength could be regarded as 0.45 ± 0.15 of the geometric mean of the preconsolidation pressure in the plane of shear and the initial mean effective stress. Most significantly, evidence is presented of a new understanding of cracking in clays. Cracks were seen to open either as pure tension cracks at zero minor principal effective stress, or as mixed-mode shear-tension cracks when an effective stress path reaches the Hvorslev criterion of brittle shear rupture, but only if the minor total stress is also tensile.

KEYWORDS: clays; cracking; negative pore pressure; suction; tensile failure

INTRODUCTION

Cracks can be initiated in clay soils during many processes, including those of desiccation, shrinkage and swelling, ice lens formation and a variety of shear deformations. Cracking is an important issue in many

La fissuration sous traction de l'argile est un phénomène important qui affecte la résistance et la perméabilité des argiles pour de nombreuses structures telles que barrages, remblais et sous-couches de décharge. Elle constitue également un précurseur de fractures de versants en terrain naturel. Cette étude examine les critères de contrainte-déformation de la fissuration dans les argiles en réalisant des essais de flexion quatre points sur des poutres en argile de kaolin consolidée. Des tests contrôlés en charge et en déformation ont été réalisés sur des poutres en argile en utilisant une succion initiale variable pour mieux comprendre les critères de contrainte-déformation d'initiation de fissure dans l'argile. La pression interstitielle négative a été maintenue inférieure à la valeur d'entrée d'air de l'argile à tout moment, de sorte que l'argile est restée continuellement saturée. Les déformations dans l'argile ont été déterminées par vélocimétrie par images de particules sur des images numériques de la poutre d'argile. Des capteurs de pression interstitielle et de tension intégrés dans les poutres d'argile ont permis d'obtenir des mesures de la succion. Les résultats de cette étude montrent que la déformation en traction seuil pour la fissuration dans l'argile de kaolin diminue de près de 4 % pour une contrainte effective moyenne initiale de 15 kPa à près de 1,5 % pour une contrainte effective moyenne initiale de 100 kPa. La contrainte extrême de la fibre à la rupture pour les poutres d'argile indiquait une résistance effective en traction correspondant à une fraction, diminuant de 0,27 à 0,11 de la pression de préconsolidation tandis que le rapport de surconsolidation augmentait de 2 à 20 environ. Une autre alternative consiste à considérer la résistance à la traction comme $0,45 \pm 0,15$ de la moyenne géométrique de la pression de préconsolidation dans le plan de cisaillement et de la contrainte effective moyenne initiale. Plus important encore, on présente ici une nouvelle approche de compréhension de la fissuration des argiles. On a pu observer la rupture de fissures résultant uniquement de la traction pour une contrainte principale mineure effective nulle ou survenant en mode mixte contrainte-tension lorsqu'un cheminement de contrainte effective atteint le critère de Hvorslev de rupture de cisaillement en régime cassant, mais seulement lorsque la contrainte mineure totale est également en traction.

Manuscript received 28 September; revised manuscript accepted 28 March 2007.

Discussion on this paper closes on 3 March 2008, for further details see p. ii.

* Schofield Centre, Department of Engineering, University of Cambridge, UK.

† Department of Civil Engineering, Queen's University, Kingston, Ontario, Canada.

engineering applications, because it adversely affects the mass strength of the material. The significance of this loss of strength is perhaps most dramatic in the case of natural clay slopes in which an essential component of their stability is derived from the clay's tensile strength accompanied by negative pore water pressures. In addition to affecting the mechanical properties, cracks also provide preferential flow paths to fluids, thus increasing the hydraulic conductivity manyfold over its previously uncracked value. This is highly significant for processes driven by infiltration (such as slope instability, water and nutrient transport for agricultural crops), and in applications in which clay has been specifically chosen for its low permeability to form all or part of a barrier system (landfill

liners, earth dams, etc.). In the vast majority of these applications the clay is above the water table, and therefore the pore water pressure is typically in suction. Despite the significance of cracking for the hydrological and mechanical behaviour of clays, relatively little experimental work has been performed to investigate the criteria for crack initiation compared with the effort expended on investigating plastic shearing.

Early work on triaxial extension tests was performed by Parry (1960) on saturated Weald clay. This work demonstrated that the failure points of saturated clay in both drained extension tests and undrained extension tests (in which the back-pressure had been elevated to maintain positive pore water pressures) satisfy Hvorslev's failure concept (Hvorslev, 1937). Tension tests on clay were also carried out by Bishop & Garga (1969), using a modified triaxial cell. They performed drained tension tests on intact samples of London clay to obtain tensile and compressive strengths expressed in terms of effective stress and the corresponding failure strains. The investigators looked to rock mechanics principles based on 'true cohesion' to analyse the results. Adopting a fracture mechanics point of view, they used modified Griffith crack theory to derive a ratio of drained tensile strength to unconfined drained compressive strength in the range 0.144–0.178, closely comparable to their test results. More recently, fracture mechanics (Harison *et al.*, 1994) and Griffith's theory have been applied to evaluate crack growth in unsaturated compacted clays (Hallett & Newson, 2001) and saturated clays (Hallett & Newson, 2005), and crack-tip stress in saturated soils (Dégué *et al.*, 2003).

Ajaz & Parry (1975) continued to work towards a strength of materials (SOM) criterion for tensile crack initiation by performing direct tension, unconfined compression and bending tests on two unsaturated compacted clays in order to investigate the stress–strain characteristics leading up to cracking. Since this research predated the development of high-capacity tensiometers, stress analysis of their results can be performed only in terms of total rather than effective stress. However, the work of Ajaz & Parry (1975) clearly demonstrated that the tensile strain at failure increased with an increase in clay moisture content, both above and below the Proctor optimum for the two compacted clays, irrespective of the type of tension test. Tensile strain at failure in a bending test was shown to increase with water content from 0.5% at a water content of about 22% to 1.5% at a water content of about 35%. These values fall within the range of tensile strains at failure extracted from the literature by Lagatta *et al.* (1997), from 1.6% in dam embankments to 4.4% in landfill clay liners. However, the need to rely on moisture content to describe the state of the clay in this work conflates the effects of void ratio and effective stress on the observed tensile behaviour, thus eliminating the possibility of deriving an SOM criterion for crack initiation. Much the same conclusion applies to work on hydraulic fracture. Murdoch (1993) investigated hydraulic fracture in clays by injecting dyed glycerine into silty clay in a triaxial cell and observing through a transparent loading plate. Results simply showed that an increase in the water content of the clay decreased the injection pressure required to initiate a hydraulic fracture in clay.

This paper presents an investigation of the stress and strain criterion for crack initiation in kaolin clay using beam bending tests equipped with embedded high-capacity tensiometers and external digital-image-based strain measurement to revisit the possibility of deriving an SOM criterion for crack initiation in clay by obtaining a full record of total and effective stresses and strains leading to failure.

EXPERIMENTAL METHODOLOGY

Flexural test set-up

The flexural test apparatus is shown schematically in Fig. 1(a) in both elevation and profile. It consists of a motorised actuator, a load cell, and four 30 mm diameter acrylic dowels to impart four-point loading. The aspect ratio of the test specimen and the positions of the loading points (Fig. 1(b)) have been selected to conform to BS 1881: Part 118, which describes the accepted procedure for performing four-point bending tests on concrete specimens (British Standards Institute, 1983). Because of the stiffness of the clay to be tested in the present study, no specific mechanical system has been included to counteract the self-weight of the clay beam. The self-weight of the beam was taken into account in the applied bending moment. In strain control tests, loading was applied at a uniform vertical displacement rate of 0.23 mm/min. In load control tests, the motorised actuator was replaced by a dead weight system and load applied in 19.6 N (2 kg) increments every 180 s. Further details of the experiment can be found in Thusyanthan (2005).

Specimen preparation

The clay to be used in the experimental programme of bending tests was chosen to be in a remoulded rather than an intact state in order to permit the creation of a large number of identical specimens, and to evaluate the zero tension line effective stress criterion often quoted for these materials. The material chosen, E-grade kaolin, is well characterised and has a liquid limit of 51%, a plastic limit of 30%, and a saturated permeability of the order of 10^{-9} m/s (Barker, 1998). The values of critical state parameters of E-grade kaolin clay acquired from various sources in the literature are summarised in Table 1. The water retention curve for E-grade kaolin is given by Rabozzi (2005); it shows an air entry suction of 250 kPa. At no time during preparation and testing was the negative pore pressure in the current tests allowed to exceed 110 kPa, so the clay can be regarded as remaining fully saturated in every case.

The powdered E-grade kaolin clay was mixed under vacuum with an equal mass of water. The resulting kaolin slurry of 100% water content was then one-dimensionally consolidated in stages to a final vertical effective stress of either 250 kPa or 500 kPa. Unloading was then performed in increments of less than 100 kPa, with swelling permitted at each stage to avoid generating large negative pore pressures, which could possibly lead to cavitation. Prior to the final unloading increment from approximately 30 kPa to 0 kPa, the specimen was isolated from all sources of water to eliminate the possibility of swelling. On unloading, the clay block was therefore forced into an initial negative pore pressure of slightly less than 30 kPa. This modest initial suction was imposed on the clay to ensure sufficient stiffness to permit undisturbed beam specimens to be cut from the large block of clay. Beams 320 mm long and of 80 mm cross-section, weighing 4 kg, were cut from the 676 mm × 200 mm × 400 mm clay block (Fig. 2(a)) and wrapped with a polythene cover for protection against evaporation. As shown in Fig. 2(b), the longitudinal direction of the beam, herein defined as the *z*-direction, has been chosen to be transverse to the direction of consolidation loading. The significance of this and of the direction of plane strain will be discussed later in the paper.

Pore pressure measurement

The ability to measure the magnitude and distribution of negative pore pressures within a clay beam is essential if an effective stress criterion is to be found for crack initiation.

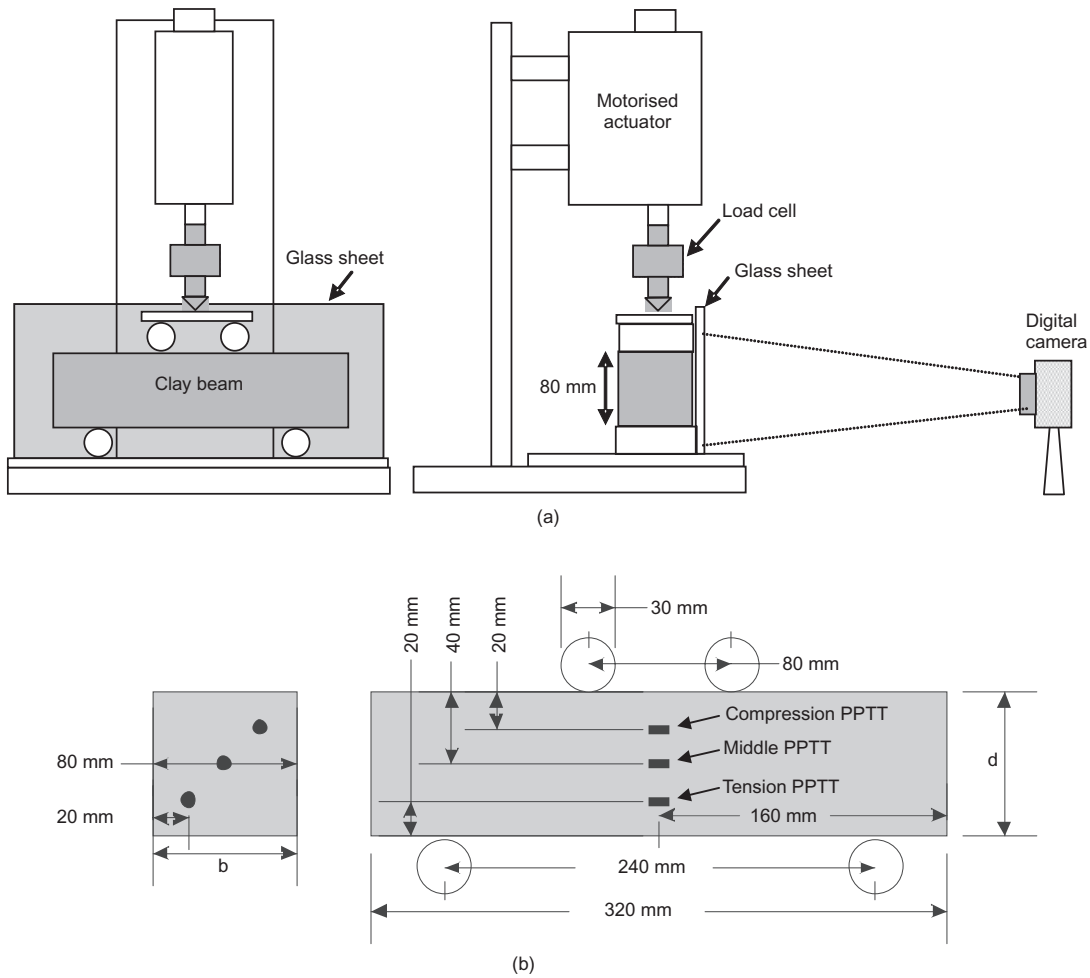


Fig. 1. Flexural test set-up: (a) elevation and profile view; (b) geometry of beam specimen

In addition to the usual challenges associated with the measurement of negative pore pressure, in this application the high-capacity tensiometers must be placed in a high effective stress environment in which they are being pinched and pulled, so they had to be designed to be insensitive to external stresses acting on the casing. In addition, they must also be small enough to be embedded in the clay beam without significantly altering the beam behaviour. Two types of high-capacity tensiometer were used in the present work: the miniature stainless steel tensiometers developed by Take & Bolton (2003), and a newly updated version of the Druck PDCR-81, which had been modified to the authors' specifications by the manufacturer to make the device more robust under tensile water pressures. The tensiometers used were about 6 mm in diameter and 10 mm long, with very flexible and slim (3 mm diameter) connecting wires.

In order to measure the evolution of the pore water pressure distribution within a clay beam during flexure, three tensiometers were embedded at the mid-span of the beam:

Table 1. Critical state parameters of E-grade kaolin clay

Parameter	Elmes (1985)*	Potter (1996)*	Present study
λ	0.124	0.124	0.124
κ	0.02	—	0.0158
Γ_{iso}	2.65	—	—
Γ_{ID}	—	2.723	2.4
M_{com}	1.05	—	0.94
ϕ_{crit}	—	—	24°

* Reported in Barker (1998).

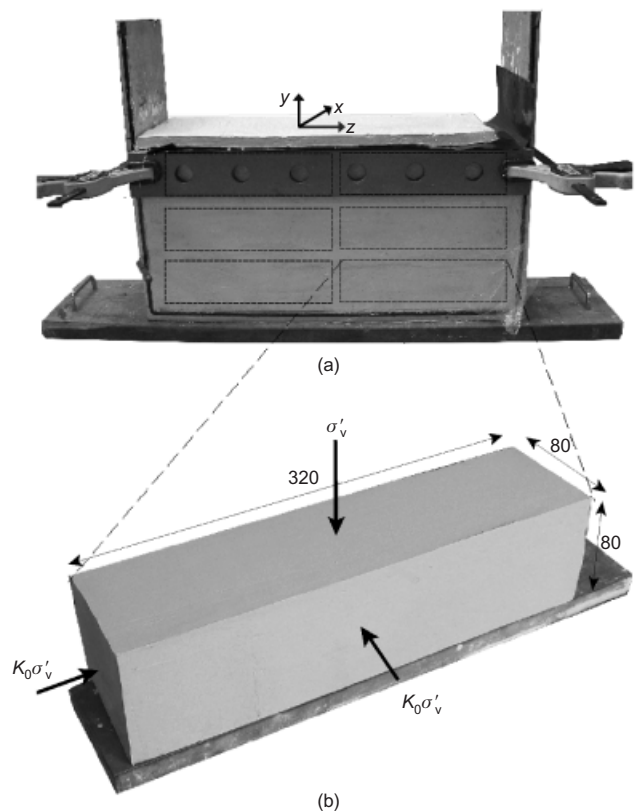


Fig. 2. Specimen preparation: (a) large block of consolidated clay; (b) 320 mm × 80 mm × 80 mm clay beam

one located near the compression face, one near the tension face, and the other near the neutral axis. As shown in Fig. 1(b), the tensiometers were positioned along a diagonal of the cross-section of the beam to mitigate their tendency to weaken the cross-section. Each tensiometer was installed in turn, beginning by slowly drilling in 1–2 mm increments from one end of the beam with a thin-walled hollow cutting tube and auger system to remove the spoil. A wooden framework and an aluminium guide were used to ensure that the drilling alignment and cover depth were consistently followed along the length of the beam. Once the hole reached the mid-span, the ceramic tip of a tensiometer that had just been saturated using the procedures of Take & Bolton (2003) was coated with a small amount of kaolin paste and inserted into the drilled hole, backfilled with a clay slurry behind the device, and allowed to set. After installation, the negative pore pressures were monitored to ensure internal consistency between the equilibrium readings of all three devices. Beams were wrapped with polythene covers during equilibration, for protection against evaporation. All three tensiometers achieved uniform initial negative pore pressures about 5 min after installation (Thusyanthan, 2005).

The inclusion of the tensiometers was essential to the research, but it was recognised that they might act as crack-raisers. After each test, photographs were taken of every fracture surface. The fracture plane was seen to intersect one or more tensiometers in 7 out of 17 tests. Equally, cracking did not coincide with the devices in 10 out of 17 tests, even though the tensiometers were located on the plane of maximum bending moment, taking both self-weight and applied loading into account. It can therefore be concluded that their influence on crack initiation could not have been significant.

Strain profile measurement

The experimental investigation of cracking described in this paper concentrates on the stress–strain behaviour of the mid-span of the beam, where the change of bending moment induced by the loading was uniform at its maximum value. The evolution of the magnitude and distribution of the longitudinal bending strain ϵ_{zz} at this location was precisely measured using the non-contact digital image correlation technique of particle image velocimetry (PIV). This technique is described by White (2002), Take (2003), and White *et al.* (2003): it allows the precise determination of soil displacements through a series of digital images without resorting to predefined target markers, instead operating on the visual image texture of the soil (colour, grain orientation, etc.). In this application, the grain size of the soil, E-grade kaolin, ensured that the natural texture of the material could be seen only at the microscopic level. Thus, using the technique described by Take (2003), an artificial texture was applied to the longitudinal elevation of the beam using dyed fine sand. As shown in Fig. 3(a), the resulting image texture is a high-contrast black-and-white random pattern ideal for PIV analysis.

As PIV operates on image texture rather than predefined target markers, the displacement of any location throughout the beam could be measured. In this application, 33 pairs of 32×32 pixel measurement patches were defined in the digital image on either side of the mid-span of the beam throughout the full height (Fig. 3(a)). Thus these pairs of displacement nodes can be thought of as 33 virtual strain gauges, which can be used to calculate the longitudinal strains throughout the depth of the beam by dividing the horizontal movement of the two patches making up each pair by the original distance between the patches (Fig. 3(b)).

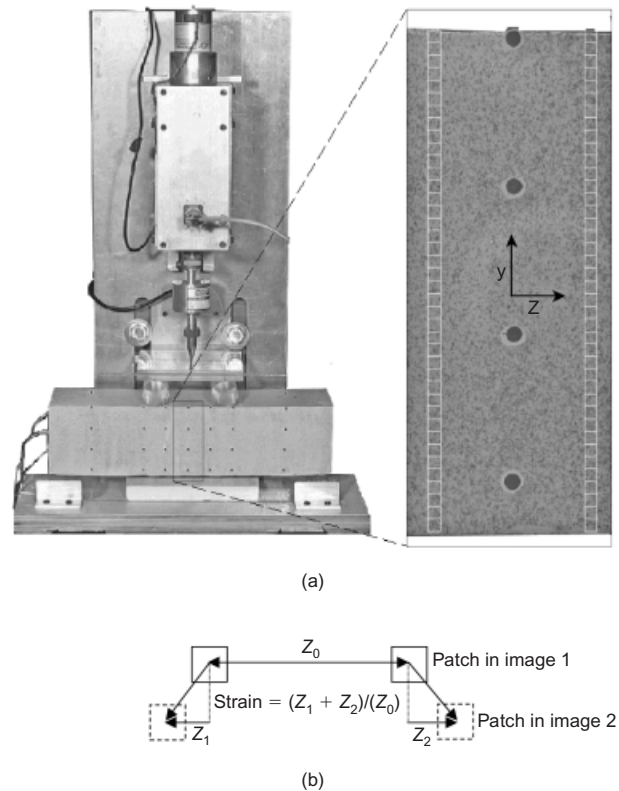


Fig. 3. Strain measurement by PIV analysis: (a) 32×32 pixel size patches at which displacement is tracked; (b) strain calculation

The error in movement measurements by PIV analysis is about $0.3 \mu\text{m}$ (White *et al.*, 2003).

Digital images of the beams were captured every 10 s during flexural testing by two 4 megapixel digital cameras: one was focused on a wide field of view to observe the behaviour of the entire beam, and the other was zoomed to capture the detailed behaviour of the mid-span. As shown in Fig. 1(a), a thin glass sheet containing a grid of black control markers at known locations was placed in front of the beam to provide a reference coordinate system visible in both cameras. This coordinate system was then used to improve the precision of the measured strains using photogrammetric camera calibration to remove camera errors such as the variation in scale factor due to imperfect camera positioning, radial and tangential lens distortion, and refraction (White *et al.*, 2003).

TESTING PROGRAMME AND EXPERIMENTAL RESULTS

The stress and strain criterion for cracking in E-grade kaolin clay was investigated for beams of varying preconsolidation pressure (type A beams having been consolidated to a vertical effective stress of 500 kPa, and type B to 250 kPa), of varying initial negative pore pressure over the range 15–102 kPa, and tested in both load and strain control. At no time did the suction exceed the air entry value of the clay, which is 250 kPa (Rabozzi, 2005). Identical experimental techniques could be used to investigate cracking under conditions of partial saturation, so long as the tensiometer filters were of sufficiently high air entry value and remained saturated. In the simpler conditions used here the clay remained saturated throughout, permitting the application of Terzaghi's effective stress principle in the analysis of the results. In particular, the initial negative pore pressure in the

unloaded beam can be simply equated to the initial mean effective stress in the clay. A full description of the 17 beam tests that have been performed for this study is included as Table 2.

Having come into moisture equilibrium following the installation of the three tensiometers, each beam was observed to have a uniform negative pore pressure profile in the range 15–30 kPa (Thusyathan, 2005). As the majority of the tests listed in Table 2 required higher initial negative pore pressures, the initial suction on the surface of the beams was set by slowly allowing controlled evaporation. Beams were rotated at regular intervals to facilitate uniform drying from all sides. Once the target value of negative pore pressure had been reached, the beams were once again covered with a protective film for an additional moisture equilibration period prior to testing. The protective film was removed just prior to testing.

As expected, all clay beams experienced brittle failure by cracking on the tensile face in the mid-span region of the beam. The load, and hence the bending moment experienced by the beams, increased up to the onset of cracking. Shortly after the initiation of a crack on the tensile face, complete collapse occurred in the load-controlled tests, whereas in the strain-controlled tests the load was observed to decrease while the crack propagated vertically upwards into the beams. Complete collapse of the beams in the strain-controlled tests was observed once the crack had propagated through about two-thirds of the beam thickness.

A summary of the maximum observed bending moment for all beams is presented in Fig. 4. In general, beams having a higher preconsolidation pressure exhibited a higher load at tensile failure. Very roughly, type A beams that had been consolidated to twice the consolidation pressure of type B beams were shown to carry a higher maximum moment in roughly the same proportion. However, this generalisation is not true for all beams. Beams with low initial effective stresses experienced similar failure loads despite their differences in preconsolidation pressure. In the following sections of the paper these experiments are analysed in detail to evaluate experimentally whether a deformation- or effective-stress-based criterion could be developed to predict this complex crack initiation behaviour.

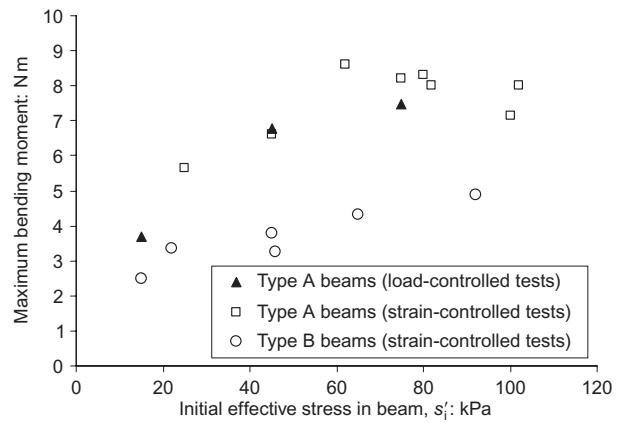


Fig. 4. Maximum bending moment applied to beams at failure

EVALUATION OF DEFORMATION-BASED CRACKING CRITERION

Observed longitudinal strains

Typical isochrones of strain calculated from the digital images record of the load-controlled and strain-controlled beam tests are presented in Figs 5(a) and 5(b) respectively. Although measurements of strain were obtained every 10 s, Fig. 5(a) shows strains only every 30 s and Fig. 5(b) every 50 s for the sake of clarity. In the load-controlled test, the strain rate was observed to be very rapid during load application, and was then followed by a period of creep strains on the order of 0.1% for the 180 s constant load period. As expected, the strain rate in the strain-controlled tests was constant until the initiation of cracking. It is clear from these results that the strain profile is almost perfectly linear with depth for both the load-controlled and strain-controlled tests up until the point of crack initiation. This confirms that the oft-made assumption that plane sections remain plane during flexural tests is valid for the present study.

The observed extreme fibre compressive and tensile strains are plotted against time in Figs 5(c) and 5(d) for the load-controlled and strain-controlled tests respectively. As shown by the symmetry of these figures, the absolute values of the compressive and tensile strains of the extreme fibres are almost identical until the point of crack initiation. This

Table 2. Test programme

Type of four-point bending test	Test	Initial suction measured, s'_i : kPa	Preconsolidation pressure, s'_0 : kPa
Load-controlled tests on clay type A beams (2 kg every 3 min)	AL15	15	297
	AL45	45	297
	AL75	75	297
	AS25	25	297
Strain-controlled tests on clay type A beams	AS45	45	297
	AS62	62	297
	AS75	75	297
	AS82	82	297
	AS80	80	297
	AS100	100	297
	AS102	102	297
	Strain-controlled tests on clay type B beams	BS15	15
BS22		22	148
BS45		45	148
BS46		46	148
BS65		65	148
BS92		92	148

A: 500 kPa consolidated beams; B: 250 kPa consolidated beams; S: strain-controlled tests; L: load controlled tests

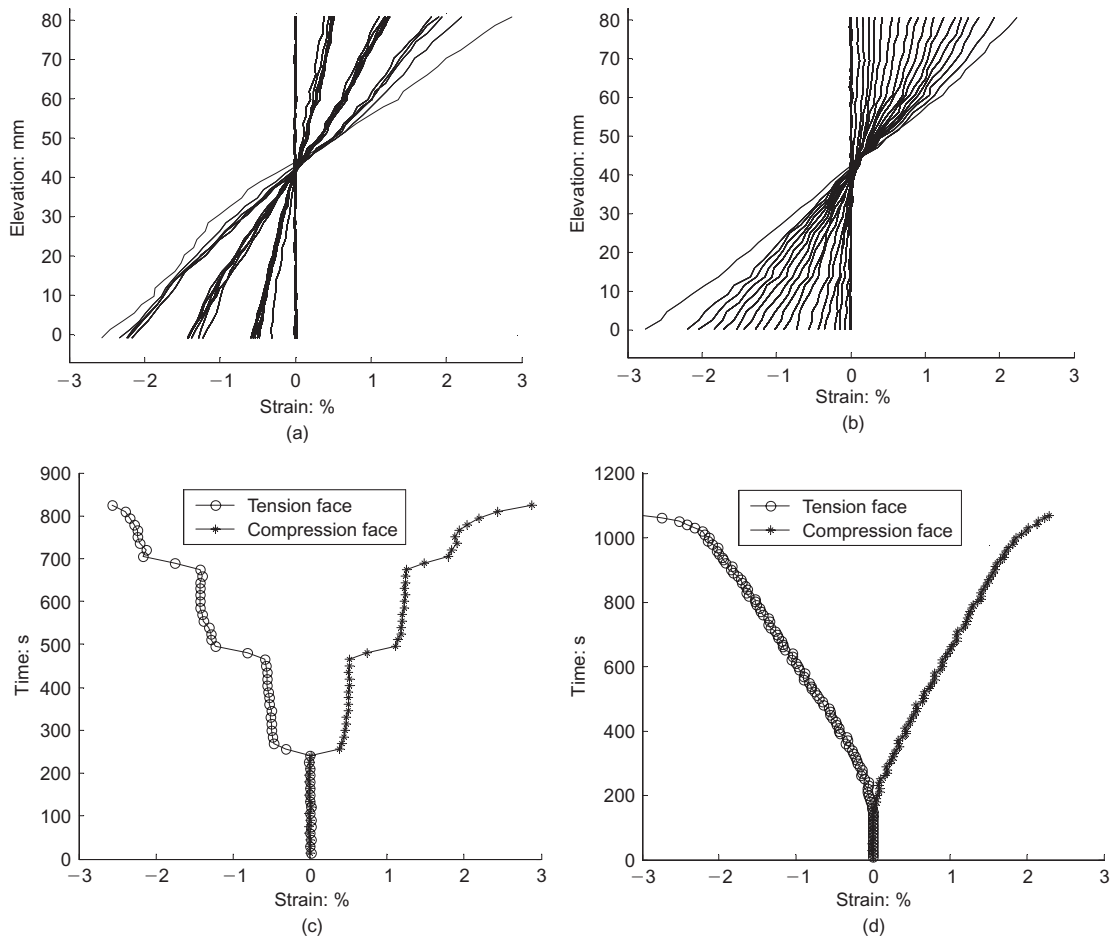


Fig. 5. Isochrones of longitudinal strain: (a) load-controlled beam AL15 strains profile every 30 s; (b) strain-controlled beam AS45 strains profile every 50 s; (c) beam AL15, extreme fibre tensile and compressive strains every 10 s; (d) beam AL45, extreme fibre tensile and compressive strains every 10 s

implies that the stiffness modulus of the clay in compression and in tension is similar in magnitude for the two tests presented in Fig. 5. The universality of this observation was tested by analysing the strain profiles from all beam tests to infer the depth of the neutral axis prior to the initiation of a crack. A neutral axis found at the mid-elevation would confirm that the two moduli are identical, whereas a neutral axis higher than mid-depth would imply a stiffer response in compression than tension.

The observed depths of the neutral axis in all beam-bending tests are plotted against the initial negative pore pressure (equal to an isotropic effective stress) present in each of the beams in Fig. 6. At the highest effective stresses, the neutral axes of the beams were found to be very close to

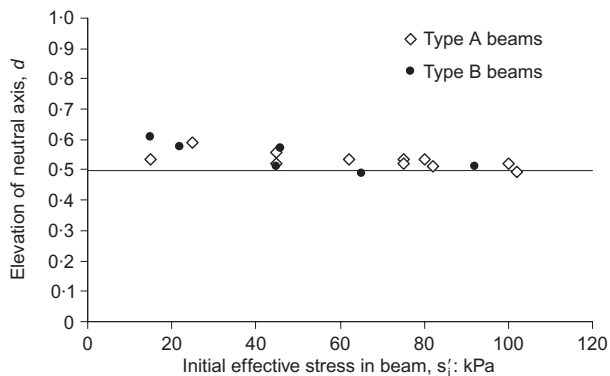


Fig. 6. Neutral axis location against initial effective stress in beam

the mid-depth. As the magnitude of the effective stress decreased, the observed neutral axes rose to become slightly higher than mid-depth. This implies that the stiffness of the clay in tension at low effective stress is lower than in compression, albeit slightly. The data also indicate that there is no significant difference between the neutral axis depth of beams consolidated to 500 kPa (type A) or to 250 kPa (type B). In all the beams, the neutral axis shifted upwards at the initiation of a crack, as expected.

Other strain components

While the bending of beams induces compressive and tensile longitudinal strains, compensating strains must simultaneously occur in the plane of the cross-section to maintain constancy of volume during an undrained increment of bending moment. Fig. 7 shows that the vertical strains, interpreted from PIV, remain a small fraction of the longitudinal strains. It must follow that the compensating strains occur across the width of the clay beams (in the *x* direction), with their magnitude roughly equal to the magnitude of the longitudinal strains, but their signs reversed. A conceptual sketch of the deformed longitudinal elevation and the cross-section of the central portion of the beam are shown in Fig. 8. It follows that an undrained deformation of the beam can be considered as the superposition of horizontal laminae, each of which deforms approximately in plane strain with the intermediate principal strain $\epsilon_{yy} \approx 0$ lying in the vertical direction. This ideal situation will not apply exactly, of course, if sufficient time elapses for drainage to take place.

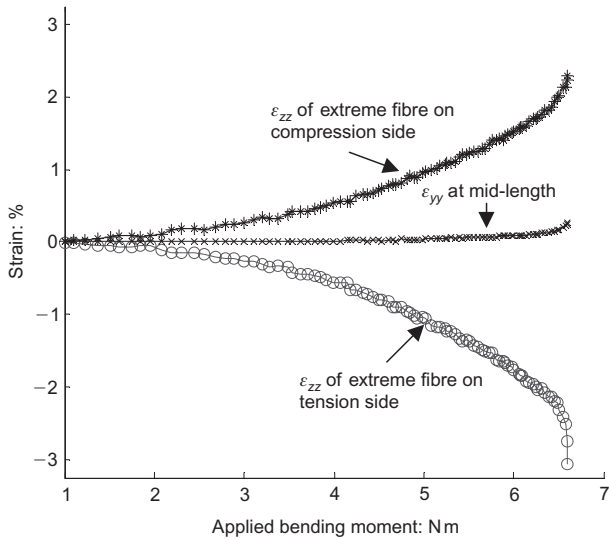


Fig. 7. Strains measured in beam AS45 at mid-length

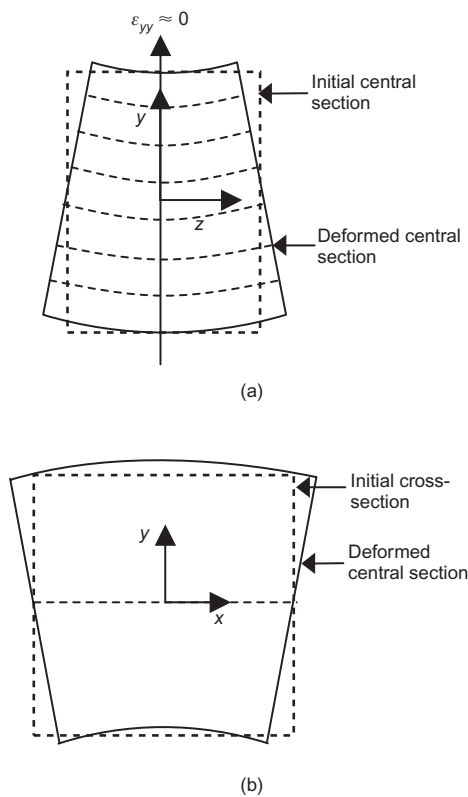


Fig. 8. Conceptual sketch of initial and deformed central portion of a beam: (a) elevation; (b) cross-section

Strain criteria for crack initiation

The measured tensile strain at the instant of crack initiation in each of the 17 beam tests is presented in Fig. 9. An equation that may be used to predict the tensile strain at which a crack initiates in clay is also given in Fig. 9 ($\epsilon_{\text{crack}} = 14s_i'^{-0.5}$). The results indicate that the tensile strain required for crack initiation in clays reduces with increasing mean effective stress, falling from about 4% at 10 kPa to about 1.5% at 100 kPa. Although the scatter in the results precludes quantitative conclusions, type B beams consistently plot at the lower end of the range of observed strain values, indicating that the tensile strain for crack initiation increases with increasing preconsolidation pressure over the range of values tested, although it is less significant than the effect of current effective stress.

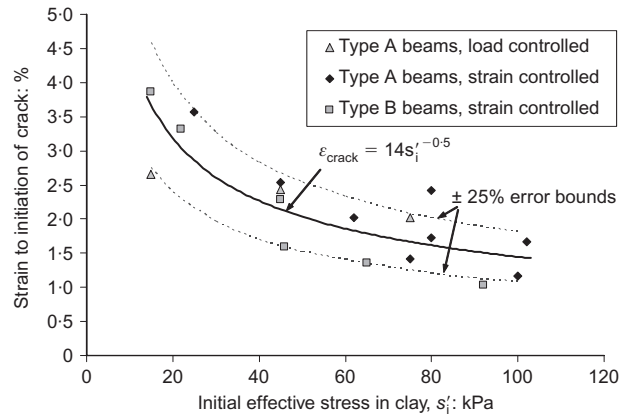


Fig. 9. Variation in tensile strain to cracking with initial effective stress

EVALUATION OF STRESS-BASED CRACKING CRITERION

Pore pressure response

A typical response from the three miniature high-capacity tensiometers embedded within the clay beam specimens during a load-controlled test is presented against time and applied bending moment in Figs 10(a) and 10(b) respectively. The immediate effect of every increment of bending was a pore pressure increase on the compression side and a

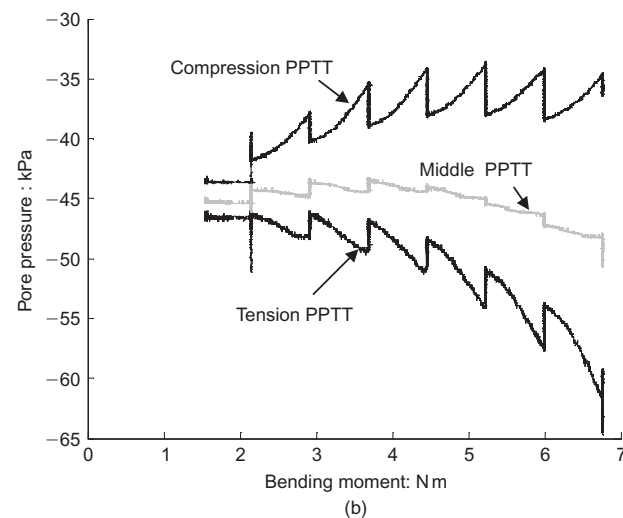
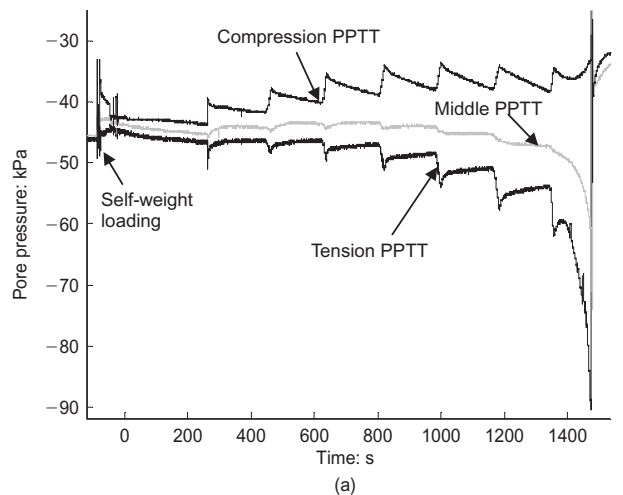


Fig. 10. Pore pressure measurements: (a) pore pressure against time in beam AL45; (b) pore pressure against bending moment in beam AL45

decrease on the tension side, as would be expected from the imposed changes of total stress. The absolute magnitude of each of these pore pressures then tended to decrease with time under constant bending moment, as would be expected by considering transient flow due to the induced excess pore pressure gradient. As the imposed total stresses were increased, the negative pore pressure increments due to tension exceeded the positive increments due to compression. At this time, the high-capacity tensiometer located at the neutral axis correspondingly begins to register a build-up of increasingly negative pore pressures. This indicates that the influence of shear-induced excess pore pressure is not symmetrical. The magnitude of the pore pressure change is larger on the tension side as additional negative pore pressures are induced due to suppressed dilation.

It is evident from Fig. 10 that the process of bending the clay beam was partially drained. Although there was negligible evaporation, there clearly was some progressive internal drainage from the compression side to the tension side. Since the objective is a description of bending and cracking in terms of effective stress changes, it is necessary only to deduce effective stress increments and relate them to strain increments. This is attempted next.

Stress distribution in the beam

The total and effective stresses imposed on the extreme tensile and compression fibres and at the neutral axis of the clay beams during flexure are shown diagrammatically in Fig. 11(a). As expected with a four-point bending test, the

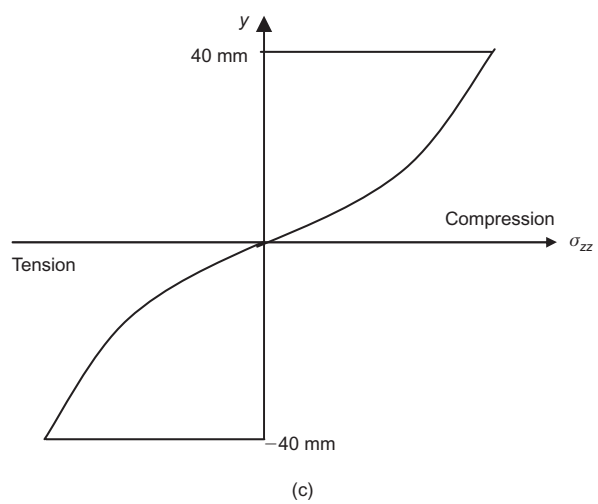
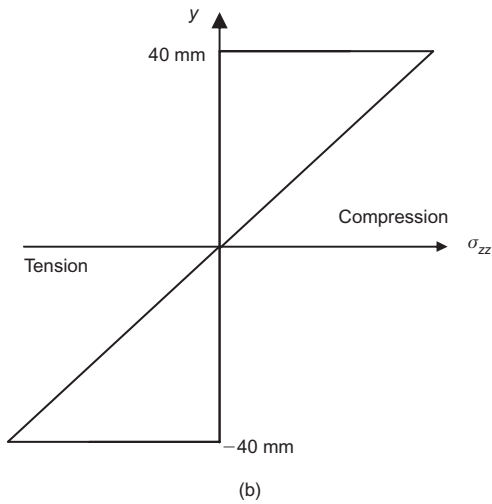
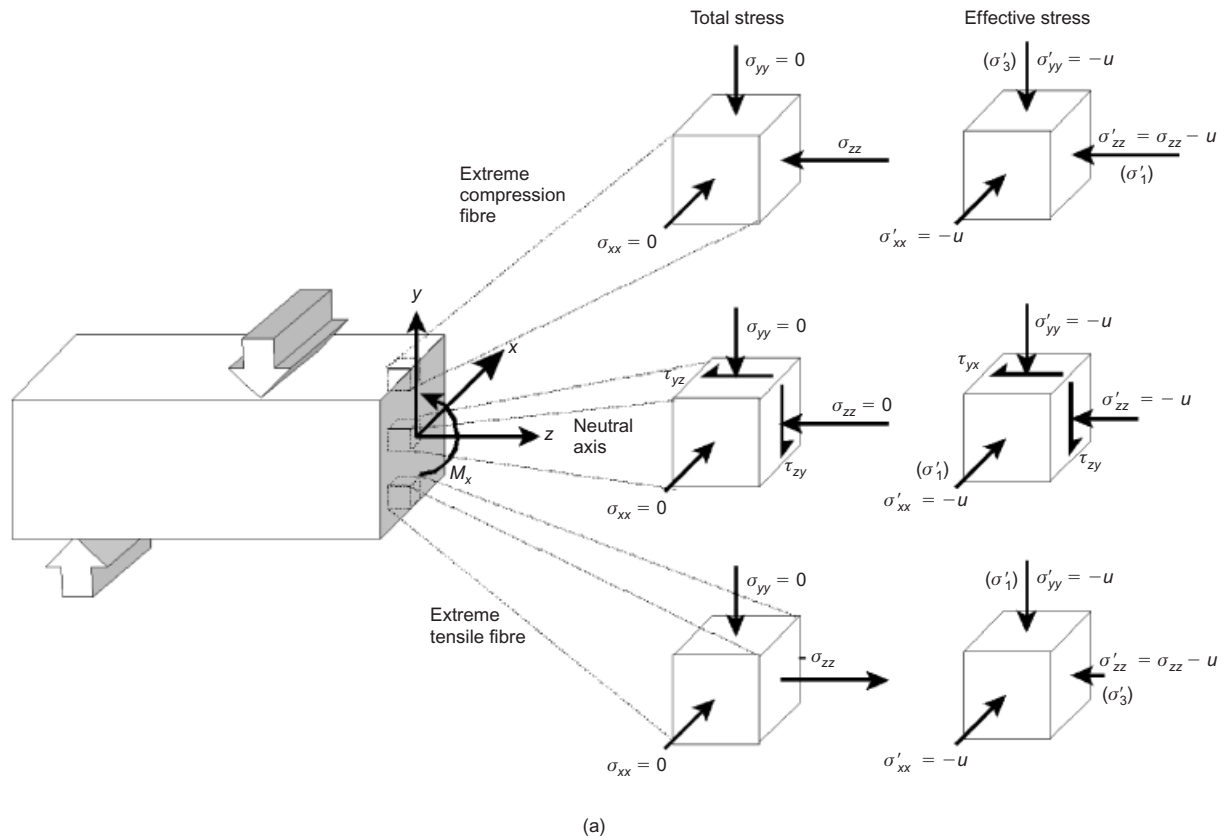


Fig. 11. (a) Principal stresses (σ_{xx} , σ_{yy} , σ_{zz}) and bending moment (M_x) in a cross-section of a beam; (b) linear elastic stress distribution; (c) non-linear elastic stress distribution

total stress in the longitudinal direction corresponds with the maximum and minimum principal stresses at the two extremities, in compression and extension respectively. Shear stresses induced at the neutral axis of the beam by four-point bending are zero. Further, the geometry of the beams has been selected so that the shear stress induced by the self-weight of the beam does not exceed 1 kPa. Shear stresses on the cross-sections are therefore negligible. As the design of the experimental study has ensured that beams have remained saturated throughout testing, the effective stresses can be determined simply by Terzaghi's equation (Fig. 11(a)).

The distribution of the longitudinal total stress in a beam of linear elastic material that is being subjected to four-point bending can be derived from elastic beam bending theory. This assumption leads to a linear stress distribution with depth as shown in Fig. 11(b). However, in the present study the beam material is overconsolidated clay, and will therefore exhibit non-linear stress-strain behaviour. The stress distribution is therefore likely to be non-linear, as shown in Fig. 11(c).

The stress distribution was not measured directly in the beam-bending experiments. However, the imposed bending moments and the precise strain distributions have been measured. Thus, if the stress-strain relationship of the overconsolidated clay were known, the measured strains could be used to infer the total stress distribution throughout the experiment. The bending moment, also known at every stage, would then offer an independent check on the validity of the stress-strain assumption.

A power law function, as given in equation (1), where C and β are parameters to be found, can be assumed to be an appropriate stress-strain relationship for overconsolidated clay (Viggiani & Atkinson, 1995; Bolton & Whittle, 1999; Atkinson, 2000). The validity of using an identical stress-strain relationship for both tensile and compressive loading has already been established earlier in the paper. This simplified total stress relation for the initial curve-fitting of the data will later be followed by an effective stress interpretation.

$$\sigma_{zz} = C \varepsilon_{zz}^\beta \tag{1}$$

Since the strain profile in the beams remains linear till near crack initiation, it is possible to use equation (2) to relate the curvature k of the beam to strain ε_{zz} .

$$\varepsilon_{zz} = ky \tag{2}$$

The assumed stress distribution and the measured curvature can be used to predict the corresponding bending moment in the beam as a function of constants C and β . The bending moment predicted by this stress distribution is given by

$$BM_{x\text{predicted}} = b \int_{-d/2}^{d/2} \sigma_{zz} y \, dy \tag{3}$$

where b is the width and d is the depth of the beam, both of which are equal to 0.08 m.

$$\begin{aligned} BM_{x\text{predicted}} &= 2b \int_0^{d/2} C(ky)^\beta y \, dy \\ &= \frac{Cbk^\beta}{2^\beta} \left[\frac{d^{\beta+2}}{\beta+2} \right] \\ &= \frac{Cbk^\beta}{2^\beta} \left[\frac{d^{\beta+2}}{\beta+2} \right] \end{aligned} \tag{4}$$

Equation (4) provides the predicted bending moment for a given C , β and k , of which the parameters C and β remain unknown. By comparing this predicted bending moment with the moment applied to the beam throughout the test, it is possible to obtain the value of parameters C and β for all the beams. In this process, the parameter C was considered to take the form $C = a(s'_0)^\alpha (s'_i)^\eta$, where a , α and η are material parameters, s'_0 is the mean effective consolidation pressure defining the yield surface (Modified Cam Clay (MCC)), and s'_i is the initial mean effective stress in the beam (i.e. the initial negative pore pressure present in the beam). The values of 0.4 for β , 2-2.5 for a , and 0.5 for α and η satisfied all the tested beams rather well. The full details of the evaluation of parameters C and β are given in the Appendix.

Using these derived parameters, the full stress distribution in the beams during flexural testing can be obtained from the observed strain profile. Fig. 12(a) shows such a plot for test AS45, in which the evolution of total stresses within the beam has been plotted every 50 s. The observed stress distribution is significantly non-linear. The total stress at the tensile face at the instant of crack initiation in this beam (the isochrone of Fig. 12(a) with the largest magnitude of stress before the strain rate jumps) was found to be -66 kPa.

Isochrones of observed pore water pressure and excess pore water pressure are given in Fig. 12(b) at corresponding

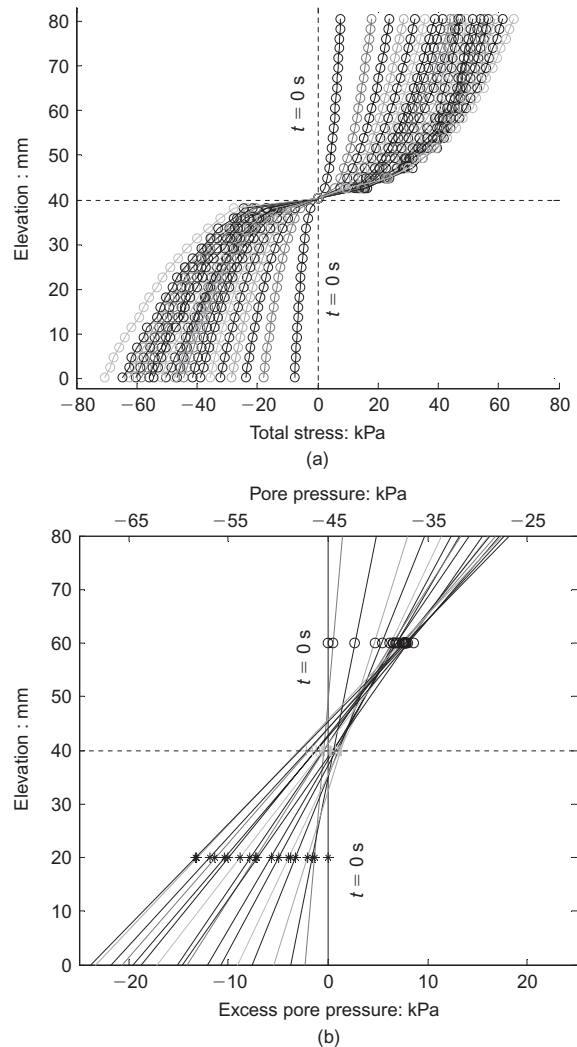


Fig. 12. (a) Stress distribution in beam AS45 (every 50 s); (b) excess pore pressure in beam AS45 (every 50 s)

times with that of the strain isochrones. As the pore water pressure was measured at only three discrete locations in the beam profile, the assumption has been made that the pore pressure distributions are linear, although it is recognised that some internal drainage may have reduced the magnitude of the excess pore pressures at the extreme fibres by a few kPa. Thus the extrapolated pore water pressure at crack initiation in this beam can be approximated as -67 kPa.

For remoulded materials, it is often assumed that tensile cracking occurs when the effective stress hits the zero tension line, $\sigma' = 0$. In the beam AS45 presented in Fig. 12(b), the effective stress at cracking was observed to be $\sigma' = \sigma - u = -66$ kPa $- (-67$ kPa) $= 1$ kPa. The zero effective stress criterion for crack initiation has therefore predicted cracking of this particular beam excellently, considering the assumptions made. This crack initiation criterion was observed to work equally well for the other beams that began with low effective stress levels.

The stress distribution for a beam of identical preconsolidation pressure but with a higher initial effective stress level (80 kPa) is presented in Fig. 13(a). This diagram is identical in shape to that of the previous beam, with the total stress at the tensile face at crack initiation now -82 kPa. The pore pressure isochrones for this beam are shown in Fig. 13(b), and indicate a pore pressure at the tensile face at crack

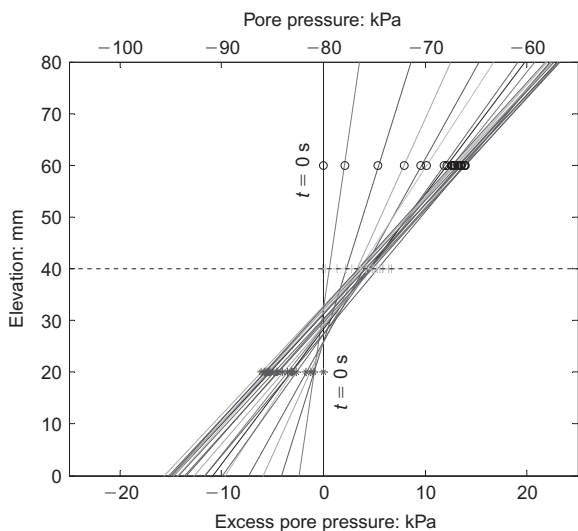
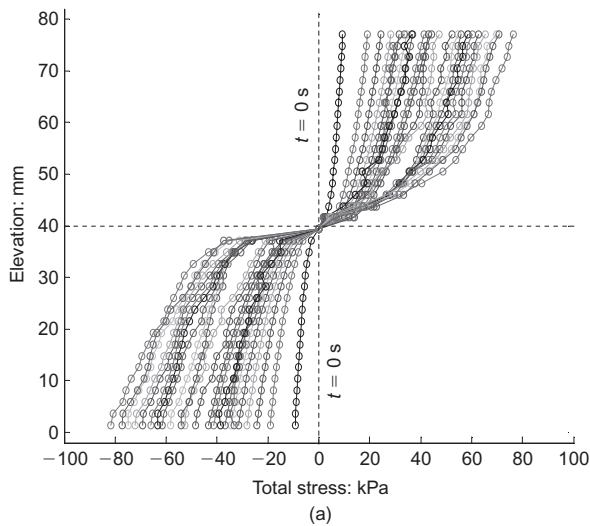


Fig. 13. (a) Stress distribution in beam AS80 (every 50 s); (b) excess pore pressure in beam AS80 (every 50 s)

initiation now -95 kPa. Thus, in terms of effective stress, this beam (AS80) has experienced crack initiation at an effective compressive stress of 13 kPa. The zero effective stress tension hypothesis was therefore not sufficient to predict cracking of clays when the soil was at moderate effective stress levels. The remaining task is to attempt a normalisation of the data so that 'low' and 'moderate' effective stress levels can be given objective definitions.

Effective stress criterion for crack initiation

In an attempt to explain the observed cracking phenomena, the behaviour will be analysed in terms of the stress paths followed by the extreme fibres of the beam. As discussed earlier, the longitudinal stresses at the extreme fibres are principal stresses, and can be calculated using equation (1) and the observed strain distribution, while the other two principal stresses σ_{xx} and σ_{yy} are equal to zero. As ϵ_{yy} was shown to be approximately zero, it follows that $t-s'$ effective stress space would be the appropriate framework for the stress paths in a horizontal lamina deforming approximately in plane strain. The shear stress t and mean effective stress s' at the two extreme fibres can be calculated as

$$t = \frac{\sigma_{zz} - \sigma_{xx}}{2} \tag{5}$$

$$s = \frac{\sigma_{xx} + \sigma_{zz}}{2} \tag{6}$$

$$s' = s - u \tag{7}$$

where u is the extrapolated pore pressure at the extreme fibre.

Using the above equations, the effective stress paths followed by the extreme tension and compression fibres up to the instant of crack initiation are presented for the load-controlled beams in Fig. 14, and for the strain-controlled beams in Fig. 15. Since the results are being plotted in $t-s'$ space, equations (5)–(7) involve only the stress components in the x and z directions. As these directions were the two K_0 directions during consolidation, it should follow that an isotropic MCC yield surface, applicable to yielding in the plane of the lamina, can be anchored through this consolidation point. Since the kaolin clay was one-dimensionally consolidated, the value of K_0 can be taken as $1 - \sin \phi_{crit}$, which is 0.593. This results in s'_0 of 297 kPa for type A beams and 148 kPa for type B beams. The yield surfaces are further annotated with the locations of the critical state line and tensile effective stress cut-off in both compression and extension.

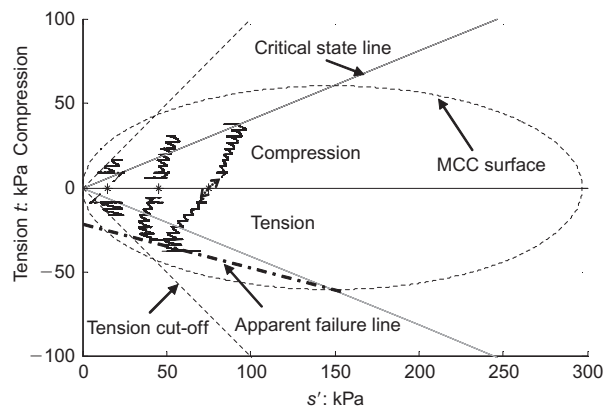


Fig. 14. Stress path to failure in load-controlled bending tests (type A beams)

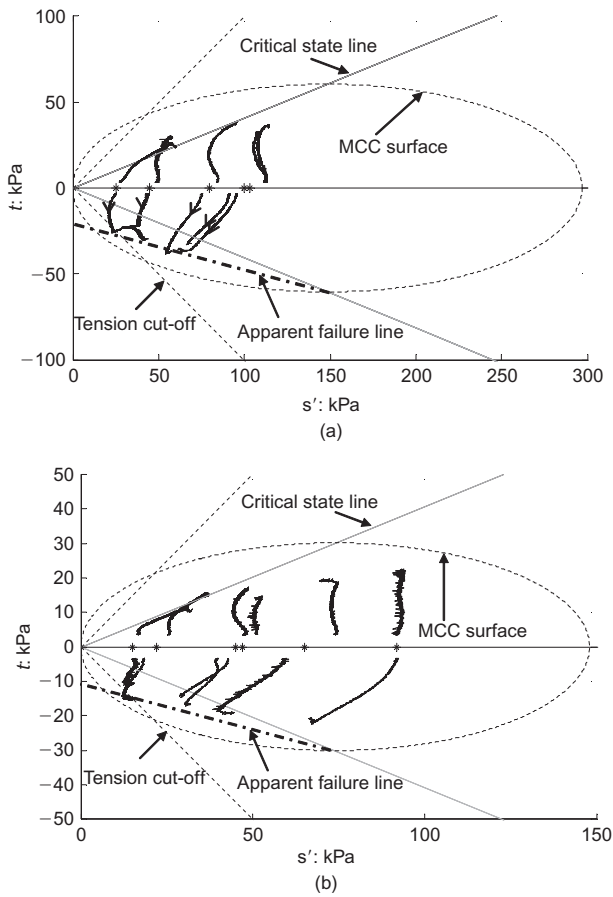


Fig. 15. Stress path to failure in strain-controlled bending tests: (a) type A beams; (b) type B beams

The initial effective stress point of each beam, within the applicable MCC yield surface, is solely a function of the initial negative pore pressure, plotted for each beam in Figs 14 and 15 as a star. Once the self-weight of the beam and the subsequent external loading are applied, the maximum shear stress within the outer compression lamina increases in the positive t direction, while that of the outer tensile lamina increases in the negative t direction. All stress paths end at the point of crack initiation at the tensile face. As shown consistently for all beams, crack initiation occurs when the stress path reaches either the tension cut-off line or an 'apparent failure line', which is akin to the usual Hvorslev line of failure states (Schofield & Wroth, 1968) observed on the compression side in normal triaxial tests. As can be seen from a summary of all results in Fig. 16, for beams with low mean effective stress cracking occurred at the tension cut-off line ($\sigma'_{zz} = 0$) irrespective of the stress history,

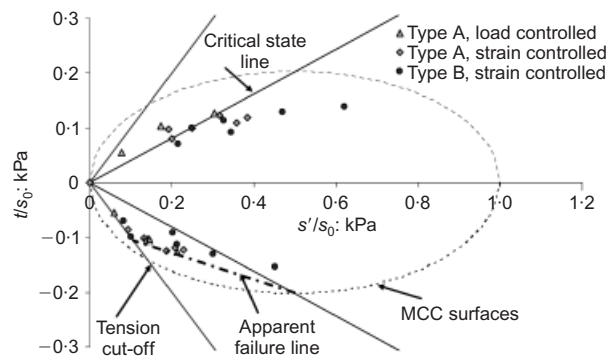


Fig. 16. Stress state of extreme fibre in tension at failure

whereas for beams with higher initial negative pore pressures, crack initiation occurred near the 'apparent failure line', which scales appropriately with the size of the MCC yield surface. Thus the stress-path analysis provides an explanation for the complex behaviour of Fig. 4, in which type A and B beams of low initial suction cracked at similar failure loads, whereas type A and B beams of higher initial suction showed a factor of almost 2 in failure loads.

The observed cracking pattern for those beams that had failed on the zero effective tension cut-off ($\sigma'_{zz} = 0$) was different from that observed for beams in which crack initiation began when the effective stress path intersected the apparent failure line. A close-up image of the mid-span of a beam that failed with effective stresses on the tension cut-off line (BS22) demonstrates that this beam has experienced Mode I fracture (Fig. 17(a)). A similar image taken from a slightly higher-suction beam (BS45) in which crack initiation occurred with effective stresses on the Hvorslev surface shows a highly inclined crack, in which both shearing and opening are occurring simultaneously (Fig. 17(b)). In other words, it is a mixed Mode I and Mode II fracture.

These observations of crack initiation are highly significant for soil behaviour. In his Rankine Lecture, Schofield (1980) proposed a simplified map of remoulded soil behaviour in which he identified three classes of limiting failure states: tensile fracture, Coulomb rupture, and ductile yielding. In his diagram, the process of tensile cracking (Mode I fracture) was confined to the region of low effective stress, shear rupture (Mode II fracture) was deemed to occur at higher effective stress levels on the dry side of critical, and the process of ductile yielding was regarded as occurring on the wet side of critical. The present study has therefore shown that what is missing from this view of soil behaviour is the shear-initiated cracking of soil on the Hvorslev surface, in total stress tension but effective stress compression.

A modified map of soil behaviour is proposed in Fig. 17(c). As before, tensile fracture (Mode I) occurs at low effective stresses, and ductile yielding at states wetter than critical. When total stress is positive (i.e. compressive), shear failure is strictly Mode II as before. When total stress is negative (i.e. tensile), shear failure will inevitably be accompanied by crack-tip opening. In other words, shear failure in this latter case will always be a mixed Mode I and Mode II fracture. This is more than just a pedantic change, as it will greatly influence cracking in regions of soil in effective stress compression, but in total stress tension such as the crests of embankments and the core of dams.

Total stress criterion for crack initiation

Although the normalised effective stress criterion presented in Fig. 16 has been shown to define the point of crack initiation, in many practical cases an estimated total stress criterion would be useful. The normalised extreme-fibre stress-strain relationship observed in the strain-controlled tests on type A and type B beams is presented in Fig. 18, along with the proposed relationship of equation (1) using the appropriate values of a (see Appendix and equation (8)). It is evident from this figure that the stress-strain behaviour of the extreme fibre agrees reasonably well with the proposed stress-strain relationship in equation (1) until the onset of cracking. Furthermore, the maximum tensile strength can be estimated as 0.45 ± 0.15 times the geometric mean of the preconsolidation pressure in the plane of shear and the initial mean effective stress:

$$\sigma_T \approx -(0.45 \pm 0.15) \sqrt{s'_0 s'_i} \tag{8}$$

Figure 19 shows the variation for all the beams of the

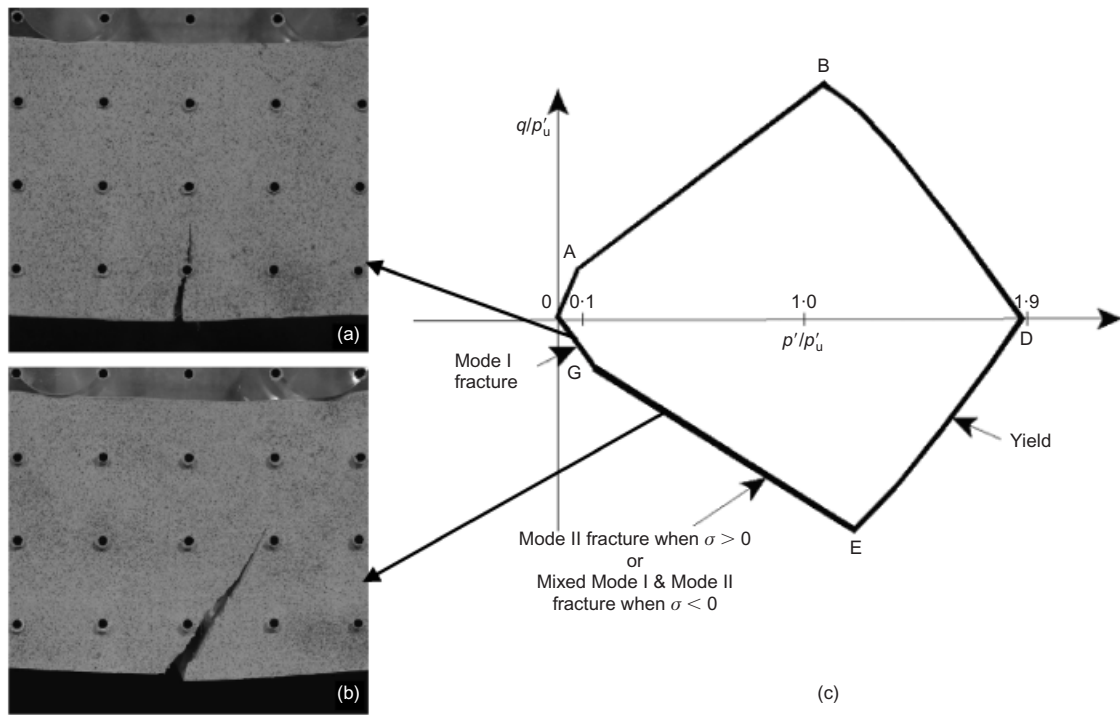


Fig. 17. Observed cracking pattern on: (a) the tensile cracking line (BS22); (b) the apparent failure line (BS45). (c) Map of soil behaviour modified from Schofield (1980)

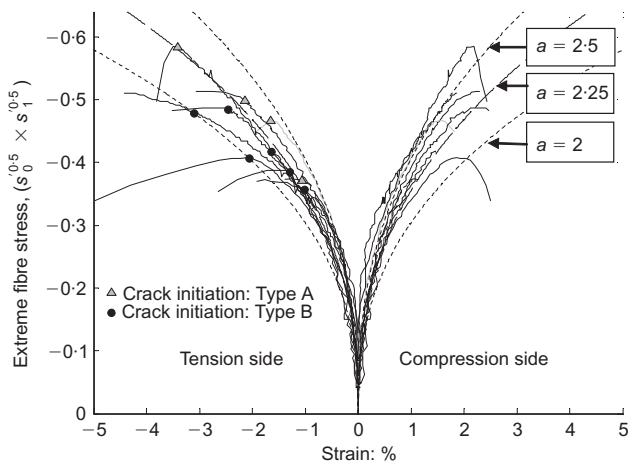


Fig. 18. Normalised extreme fibre stress against strain

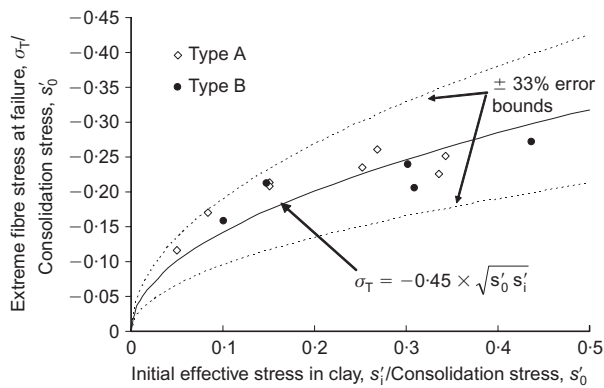


Fig. 19. Extreme fibre stress at failure/consolidation stress against initial effective stress in clay/consolidation stress

extreme fibre stress at failure plotted against the initial mean effective stress in the beam, with both axes normalised by the effective preconsolidation stress s'_0 . Equation (8) is seen to offer a trend line with reasonable bounds.

CONCLUSIONS

An investigation of the stress and strain criteria for cracking in kaolin clay has been performed using beam-bending tests equipped with embedded high-capacity tensiometers and external digital-image-based strain measurements. Load-controlled and strain-controlled bending tests were performed on clay beams with various initial suctions. Longitudinal strains along the depth of the clay beam at mid-length were obtained by PIV analysis of the digital images obtained during the bending test, and the pore pressures were measured by the pore pressure and tension transducers (PPTTs) within the beams.

Strain plots obtained in both load-controlled tests and strain-controlled tests showed linear variation with depth until near the initiation of a crack. The strain plots also showed that the neutral axis remained at or close to the mid-depth of the beam until the initiation of a crack. The strain to crack initiation was shown to be a strong function of initial mean effective stress in the clay beam. The strain level for crack initiation decreased from about 4% at 10 kPa to about 1.5% at 100 kPa. The tensile strength (in total stress) for the range of kaolin beams tested in the present study could be written as $-0.45\sqrt{s'_0 s'_i} \pm 33\%$.

The stress states of the extreme fibre in tension of all the beams at initiation of a crack showed that cracks initiated when the effective stress state reached either the tension cut-off line for low mean effective stresses or the 'apparent failure line' for higher mean effective stresses corresponding to Hvorslev's normalisation of the Mohr-Coulomb failure envelope. These effective stress criteria for crack initiation have been derived only from tests on remoulded saturated clays. However, the discovery of a crack-opening criterion

apparently coincident with the brittle shear failure criterion can reasonably be regarded as more universally significant. When total stress was negative (i.e. tensile), it was demonstrated that crack initiation would occur by shear failure and as such will always be a mixed Mode I and Mode II fracture.

This work clarifies that all states of clay on the 'dry' side of critical states are brittle, and liable to crack opening. If sheared, they approach brittle shear rupture with an effective stress criterion already known as Hvorslev's normalisation of the Mohr-Coulomb failure surface. If stretched, uncemented overconsolidated soils with small negative pore pressure approach failure at zero tensile effective stress. In either case, cracks may open if the total stress is also tensile.

ACKNOWLEDGEMENTS

The authors would like to thank all staff at the Schofield Centre, and especially the Chief Technician, Chris Collison, and Frank Sixsmith for their help with the experimental set-up. This work has been funded by EPSRC Award GR/R91830/01 and a Gates Cambridge Scholarship awarded to the first author.

APPENDIX: CHOOSING PARAMETERS *C* AND β

The bending moment in the beam was calculated from the measured loads applied to the beam. The proposed equation (1) ($\sigma = C\varepsilon^\beta$) has two variables *C* and β , which have to be determined to define the stress-strain relationship of the clay. For a given *C* and β , the bending moment can be predicted using equation (3). The parameters *C* and β can be varied independently, and for each combination of chosen values of *C* and β the predicted bending moment can be compared with the measured bending moment. These parameters are chosen such that the experimental bending moments match the predicted bending moments. Fig. 20(a) shows the comparison of predicted bending moment with the experimental bending moment of beam AS45, for varying values of β ($\beta = 0.3, 0.4, 0.5$ and 0.6) and a fixed value of *C* (*C* = 300 kPa). It can be seen that, for a value of $\beta = 0.4$, the predicted bending moment matches quite well with the experimental bending moment. Fig. 20(b) shows the comparison between predicted and experimental bending moments for varying values of *C* (*C* = 150, 300, 450 and 600) and a fixed value of β ($\beta = 0.4$). The various combinations of values of *C* and β were analysed, and the best match between predicted and experimental bending moment was obtained for a value of *C* = 300 kPa and $\beta = 0.4$, as shown in Figs 20(a) and 20(b).

The value of β is expected to be the same for all the beams, whereas the value of *C* is expected to vary from beam to beam. The comparison between predicted and experimental bending moments of all the beams confirmed that the best match was obtained for a β value of 0.4 and various *C* values (Fig. 21).

The value of *C* is expected to depend on mean preconsolidation pressure (s'_0) and initial mean effective stress (s'_i). Since there is no total stress in the beam initially, the mean effective stress is equal to the negative pore pressure present in the beam. The parameter *C* can be related to preconsolidation pressure (s'_0) and initial mean effective stress (s'_i) by equation (9), where *a*, α and η are constants to be found.

$$C = a(s'_i)^\alpha (s'_0)^\eta \tag{9}$$

$$\log C = \log a + \alpha \log s'_i + \eta \log s'_0 \tag{10}$$

Since the values of *C* for all the beams have already been obtained, equation (10), which is the logarithm of equation

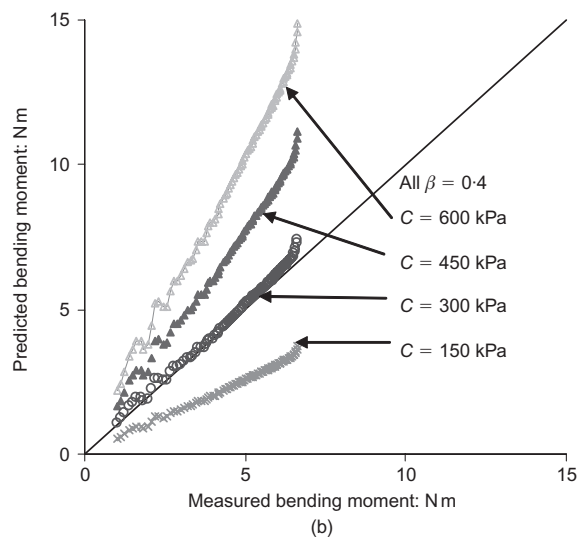
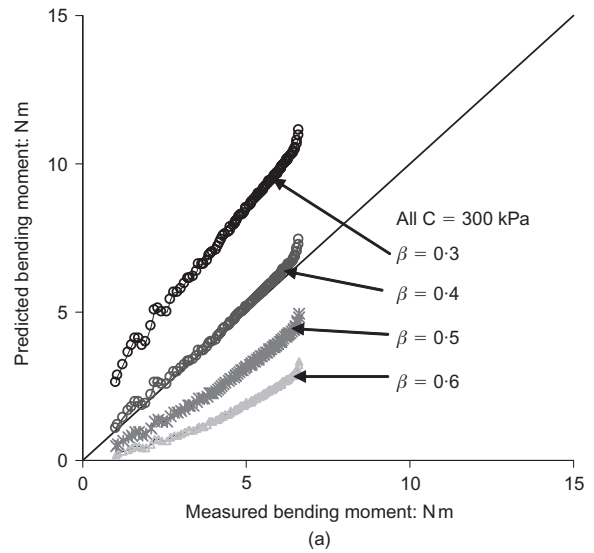


Fig. 20. Finding parameters *C* and β

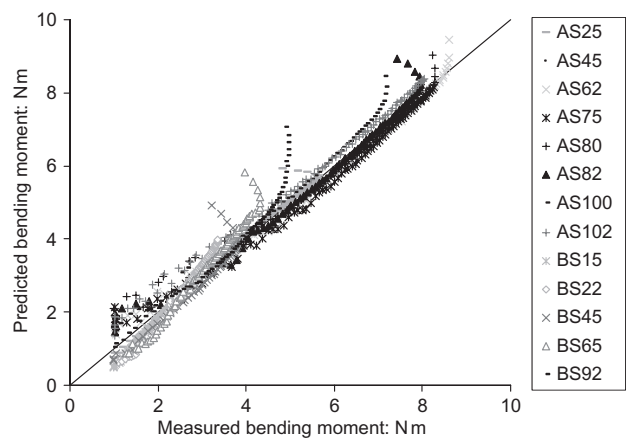


Fig. 21. Comparison of predicted and applied bending moment

(9), can be used to find the values of α and η . Fig. 22(a) shows the graph of $\log C$ against $\log s'_0$ and Fig. 22(b) shows the graph of $\log C$ against $\log s'_i$. It is clear from these graphs that the values of α and η can each be taken as 0.5. A value of *a* in between 2 and 2.5 satisfies equation (9) for all the beams.

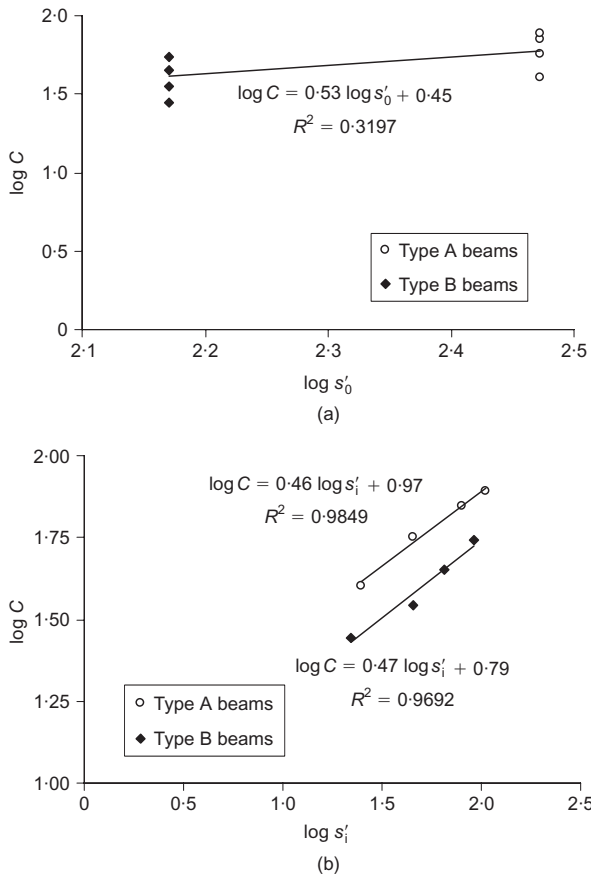


Fig. 22. Finding the value of parameters α and η

NOTATION

- a non-dimensional factor relating C to s'_0 and s'_i
- b width of clay beam (0.08 m)
- $BM_{x\text{predicted}}$ bending moment predicted from measured strain and proposed stress-strain relationship
- C parameter relating σ to ε^β
- d depth of clay beam (0.08 m)
- k curvature
- LL liquid limit
- $M_{\text{com}}, M_{\text{ext}}$ compression and tension slopes in q against p'
- PL Plastic limit
- p' effective mean normal stress $(\sigma'_{xx} + \sigma'_{yy} + \sigma'_{zz})/3$
- q deviatoric stress in triaxial loading $(\sigma'_{axial} + \sigma'_{radial})$
- s' mean effective stress $(= (\sigma_{xx} + \sigma_{zz})/2)$
- s'_i initial mean effective stress of the clay beam
- s'_0 mean preconsolidation pressure
- t shear stress $(= (\sigma_{xx} - \sigma_{zz})/2)$
- u pore pressure
- y distance from neutral axis of the beam
- α exponent of s'_i in relating C to a , s'_0 and s'_i
- β exponent of s'_0 in relating C to a , s'_0 and s'_i
- Γ_{iso} specific volume at mean effective stress of 1 kPa for isotropic compression
- Γ_{1D} specific volume at mean effective stress of 1 kPa for one-dimensional compression
- ε normal strain ($\varepsilon_{\text{crack}}$ = strain at crack initiation)
- κ slope of elastic compression line
- λ slope of plastic normal compression line
- σ normal stress
- σ'_{vc} unconfined compression stress
- σ'_{vt} unconfined tension stress
- $\sigma_{xx}, \sigma_{yy}, \sigma_{zz}$ principal total stresses
- τ shear strain
- ϕ_{crit} critical state friction angle

REFERENCES

Ajaz, A. & Parry, R. H. G. (1975). Stress-strain behaviour of two compacted clays in tension and compression. *Géotechnique* **25**, No. 3, 495-512.

Atkinson, J. H. (2000). Non-linear soil stiffness in routine design. *Géotechnique* **50**, No. 5, 487-508.

Barker, H. R. (1998). *Physical modelling of construction processes in the Mini-Drum centrifuge*. PhD dissertation, Cambridge University, UK.

Bishop, A. W. & Garga, V. K. (1969). Drained tension tests on London clay. *Géotechnique* **19**, No. 2, 309-313.

Bolton, M. D. & Whittle, R. W. (1999). A non-linear elastic/perfectly plastic analysis for plane strain undrained expansion tests. *Géotechnique* **49**, No. 1, 133-141.

British Standards Institute. (1983). *Testing concrete. Method for determination of flexural strength*, BS1881: Part 118. Milton Keynes: BSI.

Dégué, K. M., Soulié, M. & Ladanyi, B. (2003). Extension of the Griffith's fracture theory to saturated clays. *Int. J. Numer. Anal. Methods Geomech.* **27**, No. 4, 275-288.

Elmes, D. R. (1985). *Creep and viscosity in two clays*. PhD dissertation, University of Cambridge, UK.

Hallett, P. D. & Newson, T. A. (2001). A simple fracture mechanics approach for assessing ductile crack growth in soil. *Soil Sci. Soc. Am. J.* **65**, No. 4, 1083-1088.

Hallett, P. D. & Newson, T. A. (2005). Describing soil crack formation using elastic-plastic fracture mechanics. *Eur. J. Soil Sci.* **56**, No. 1, 31-38.

Harrison, J. A., Hardin, B. O. & Mahboub, K. (1994). Fracture toughness of compacted cohesive soils using ring test. *ASCE J. Geotech. Engng* **120**, No. 5, 872-891.

Hvorslev, M. J. (1937). *Über die Festigkeitseigenschaften gestorter bindiger Boden* (The physical properties of remoulded cohesive soils). Thesis published by Danmarks Naturvidenskabelige Samsfund, *Ingeniørvidenskabelige Skrifter*, Series A, No. 45, Copenhagen.

LaGatta, M. D., Boardman, B. T., Cooley, B. H. & Daniel, D. E. (1997). Geosynthetic clay liners subjected to differential settlement. *J. Geotech. Geoenviron. Engng* **123**, No. 5, 402-410.

Murdoch, L. C. (1993). Hydraulic fracture of soil during laboratory experiments. Part 1: Methods and observations. *Géotechnique* **43**, No. 2, 255-265.

Parry, R. H. G. (1960). Triaxial compression and extension tests on remoulded saturated clay. *Géotechnique* **10**, No. 4, 160-180.

Potter, L. J. (1996). *Contaminant migration through consolidating soils*. PhD dissertation, University of Cambridge, UK.

Rabozzi, C. (2005). Evaluation of mineral barriers water retention curves using the vapour equilibrium method. *Proc. 10th Int. Workshop on the Hydro-Physico Mechanics of Landfills, Grenoble*.

Schofield, A. N. (1980). Cambridge geotechnical centrifuge operations. *Géotechnique* **30**, No. 3, 227-268.

Schofield, A. N. & Wroth, C. P. (1968). *Critical state soil mechanics*, Chapter 8. McGraw-Hill (now available as a pdf download from <http://www.geotechnique.info/>).

Take, W. A. (2003). *The influence of seasonal moisture cycles on clay slopes*. PhD dissertation, University of Cambridge, UK.

Take, W. A. & Bolton, M. D. (2003). Tensiometer saturation and reliable measurement of soil suction. *Géotechnique* **53**, No. 2, 159-172.

Thusyanthan, N. I. (2005). *Behaviour of landfill systems under monotonic and earthquake loadings*. PhD dissertation, University of Cambridge, UK.

Viggiani, G. & Atkinson, J. H. (1995). Stiffness of fine-grained soil at very small strains. *Géotechnique* **45**, No. 2, 249-265.

White, D. J. (2002). An investigation into the behaviour of pressed-in piles. PhD dissertation, University of Cambridge, UK.

White, D. J., Take, W. A. & Bolton, M. D. (2003). Soil deformation measurement using particle image velocimetry (PIV) and photogrammetry. *Géotechnique* **53**, No. 7, 619-631.